Simultaneous measurement of circular dichroism and Faraday rotation at terahertz frequencies using heterodyne detection

G. S. Jenkins,[1] D. C. Schmadel,[1] and H. D. Drew[1]
Center for Nanophysics and Advanced Materials
Department of Physics, University of Maryland, College Park, Maryland 20742, USA

(Dated: 31 May 2010)

A far-infrared system measures the full complex Faraday angle, rotation as well as ellipticity, with an unprecedented accuracy of 10 μrad/T. The system operates on several far-infrared laser lines in the spectral range from 0.3 to 6 THz and produces results as a continuous function of temperature from 10 to 310K and applied fields between $\pm$ 8 T. Materials successfully measured include GaAs 2-DEG heterostructures, various high temperature superconductors including $Bi_2Sr_2CaCu_2O_{8+x}$, $Pr_{2-x}Ce_xCuO_4$, and $La_{2-x}Sr_xCuO_4$, and single crystals of the topological insulator Bi_2Se_3.

PACS numbers: 78.20.Ls,78.66.Bz,74.25.Gz,74.72.-h,
Keywords: Faraday effect, ellipticity, circular dichroism, Terahertz, heterodyne detection

arXiv:1005.5196v1 [cond-mat.str-el] 28 May 2010

I. INTRODUCTION

Hall effect measurements are a powerful tool routinely used in condensed matter physics. Extension of these measurements to optical frequencies provides dynamical characterization of the off-axis conductivity σ_{xy} where optical propagation is in the z direction. This off-axis conductivity when combined with the longitudinal conductivity σ_{xx} from standard optical measurements produces the full complex conductivity tensor along with the Hall angle defined as $\tan(\theta_H) = \sigma_{xy}/\sigma_{xx}$.

This additional information available from infrared (IR) Hall measurements has been particularly useful in investigating strongly interacting electron systems, materials often defying paradigms in condensed matter physics established in the twentieth century. Since interaction effects can enter into σ_{xy} differently than σ_{xx},[1,2] the IR Hall effect provides new insights to strong correlation physics. Similar to σ_{xx}, Hall spectroscopy probes the energy scales of the system including energy gaps and carrier scattering rates. It also obeys sum rules that permit a more global view of the effects of the interactions on the electronic structure of materials.[1,3,4] IR Hall measurements have led to several recent important findings: refuting the spin-charge separation scenario for the anomalous behavior of the dc Hall effect in cuprates,[1,5,6] firmly establishing that the anomalous dc Hall effect in the paramagnetic state of n-type and p-type cuprates is caused by current vertex corrections produced by electron-electron scattering mediated by antiferromagnetic fluctuations,[7–9] observing the first evidence of small Fermi pockets in underdoped cuprates,[10] demonstrating that inelastic scattering enters into the Hall conductivity differently than the longitudinal conductivity,[5,6] and characterizing the Fermi pockets formed by a spin density wave gap in underdoped $Pr_{2-x}Ce_xCuO_4$.[4,7]

Hall effect measurements at very low optical excitation energies in the THz spectral region probe intrinsic properties associated with the Fermi surface (FS) which are sensitive to the FS topology as well as Fermi velocity and scattering rate anisotropies.[7–9] One of the advantages of the far-IR (FIR) Hall measurements over the mid-IR (MIR) Hall measurements[11] is that for many material systems, there are known intermediate energy scales between 10 and 100 meV which make comparison between MIR Hall measurements difficult with dc transport and other low frequency probes.

Important future applications include extending quantum Hall effect (QHE) measurements to the THz regime. The recent appearance of novel 2-D systems such as graphene and the conducting surface states on topological insulators (TI) has stimulated interest in the transport and magneto-transport in systems with "massless" Dirac electronic dispersion. Topological insulators are predicted to form a new 2-D quantum state of matter fundamentally related to the edge states in the QHE.[12] Although many exotic properties are predicted, of particular interest are signatures at finite frequencies of a quantum Hall step $\sigma_{xy} = (1/2)e^2/h$ – even though there exist no edge states – never before observed. For that matter, the frequency dependence of the QHE has never been measured in any material at optical frequencies, a topic we are currently pursuing. In particular, the Faraday angle in both graphene and TIs is predicted to be quantized in units of the fine structure constant.[12–14]

The instrument to be described in the following pages is capable of measuring the full complex Faraday angle defined as:

$$\tan\theta_F \equiv \frac{t_{yx}}{t_{xx}} \tag{1}$$

where t_{yx} and t_{xx} are the transmission amplitudes through the sample, which is situated in a magnetic field perpendicular to its surface and parallel to the propagation direction of the optical beam. The system operates on various laser lines in the terahertz spectral region (0.3 to 6 THz) and produces data to an unprecedented accuracy of 10 μrad/T and as a continuous function of

temperature from 10 to 310 K. Using the full complex Faraday angle, together with independent measurements of the longitudinal conductivity σ_{xx}, one may then calculate both the the complex Hall angle and σ_{xy}.

In what follows we shall first present an overview of the system followed by a detailed examination of several of the more critical components and design issues. Finally, we discuss the system calibration and operation. Useful mathematical notation and models appear in the appendices.

II. INSTRUMENT OVERVIEW

Fig. 1 presents a schematic representation of the system. At the beginning of the optical path, a chopped, continuous wave CO_2 laser pumps a single longitudinal mode, far-infrared (FIR), molecular vapor laser which is the source of the THz radiation. An aluminum parabolic mirror focuses the output of the FIR laser onto a pinhole aperture to remove spatial noise. A second aluminum parabolic mirror collimates the emerging beam and directs it into a beam steering assembly consisting of two flat mirrors. Next, an aperture stop reduces the beam diameter to a size so that the radiation does not encounter the sides of the bore tube of the mechanical rotator. A thin mylar sheet beam splitter splits off a small portion of this reduced diameter beam for use as a power reference. The main portion of the reduced diameter beam passes through the mylar beam splitter and enters the bore of the high speed mechanical rotator. A waveplate mounted within the bore typically spinning at ∼3000 RPM modulates the beam so as to introduce various harmonics of the rotation frequency into the polarization states. A third aluminum parabolic mirror focuses the beam onto the sample located in a ±8 Tesla superconducting Helmholtz magnet. The magnetic field is aligned parallel to the beam path.

In the Faraday geometry, the portion of the beam transmitted by the sample passes through an analyzer polarizer and onto a fourth aluminum parabolic mirror, which re-collimates it. A fifth aluminum parabolic mirror focuses the beam into the output detector. Note that the beams leading to and from the magnet and the fourth and fifth mirrors are collimated. This allows increasing the separation between the magnet and the detector and laser source so as to reduce the effects of the strong magnetic field upon these components. Also note that, except for the small amount of spatial noise introduced by the aperture stop prior to the mechanical rotator, the system operates essentially within a single spatial mode. This limits noise from modal interference whose frequencies resulting from vibration, thermal drifting, etc. would otherwise fall within the mechanical rotator frequency and its harmonics.

An ideal rotating waveplate transmits linearly polarized light when either the ordinary or extra-ordinary axis aligns with the polarizer. This occurs four times per revolution of the waveplate giving rise to a fourth harmonic signal. With a moments thought, one will recognize that a sample inserted in the magnet so as to cause a real Faraday rotation $\mathrm{Re}(\theta_F)$ will change the relative phase of this fourth harmonic. In fact, the fourth harmonic phase change is directly proportional to the Faraday rotation. An angular position sensor on the mechanical rotator allows determination of this phase change.

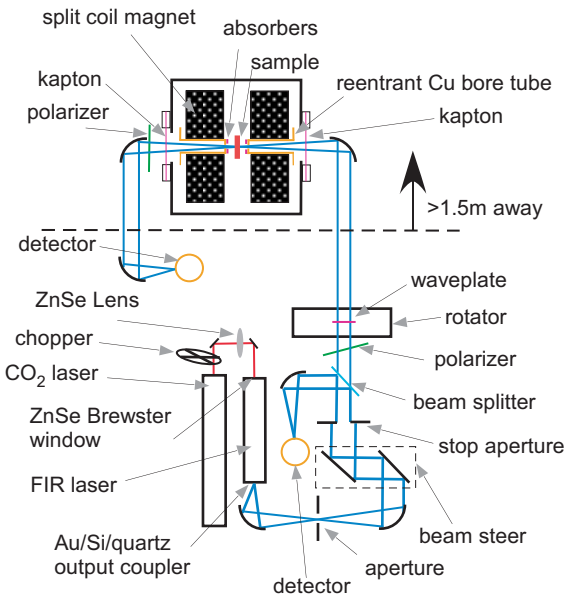

FIG. 1. (Color online) Schematic of the complex Faraday angle measurement system operating on various laser lines in the THz region.

Considering no sample in place, the polarization state oscillates between pure left and right handed circular polarized light twice upon one full rotation of an ideal waveplate. Upon introduction of a sample, one can see qualitatively that the second harmonic signal is then sensitive to the induced ellipticity or circular dichroism. The appendix presents, in a very manageable notation, a complete derivation of all the various signals one might expect for typical samples. Corrections to accommodate errors and losses in the various system components is accomplished via an *in situ* calibration technique discussed in Sec. IV C.

In general, a sample induces polarization rotation, characterized by $\mathrm{Re}(\theta_F)$, as well as ellipticity, characterized by $\mathrm{Im}(\theta_F)$. The resulting signals recorded at the output detector include dc level R_{dc} of the transmittance through the sample measured at the chop frequency ω_{chop} of the CO_2 pump laser and $A_{i,2\omega}$, $A_{o,2\omega}$, $A_{i,4\omega}$, and $A_{o,4\omega}$, which are the second and fourth harmonic signals on the output detector that are in-phase (i) and out-of-phase (o) with the original harmonic signal that results when no sample is present or when the magnetic field is zero. By

taking appropriate ratios of $A_{i,2\omega}$, $A_{o,2\omega}$, $A_{i,4\omega}$, $A_{o,4\omega}$, and R_{dc}, one may extract the complex Faraday angle via Eq. A2. Note that similar to heterodyne detection schemes, for small angles the desired quantities are proportional to the phase and therefore the transverse t_{xy} amplitude rather than being proportional to the power which is not so accurately measured for small values.

III. CRITICAL COMPONENTS AND DESIGN ISSUES

A. Etalons and Multiple Reflections

Multiple reflections within optical elements and between optical elements can result in spurious signals and must be minimized. Consider, for example, that the Faraday effect accumulates regardless of the direction of the light beam. Whereas a single pass through a sample or optical element may produce a rotation of θ, a pass forward, then backward, then again forward will produce a rotation of 3θ. This is a concern not only for the sample but for any optic within the magnetic field, for which reason we use thin polyimide film, 25 micron, as the magnet vacuum windows. Even outside of the magnetic field multiple reflections can cause small variations over time due to very small motions or vibrations of the hardware like flexing of the magnet cryostat or flexing of the the aluminum optical table from cryogen boil-off, motion of the floor, thermal drift, etc.

To control these effects, optical elements may be: chosen to be much thinner than the wavelength; conditioned with an antireflection (AR) coating; and/or set at an angle to the optical path. For example, a dielectric AR layer was utilized on an $LaSrGaO_4$ (LSGO) substrate to impedance match between vacuum and the FIR substrate index of $n \approx 4.4$. The matching layer was a piece of z-cut quartz chemically etched to a thickness equal to an odd multiple of a quarter wavelength and held against the substrate by means of a spring. The refractive index of quartz in the FIR is 2.12 which is close to the geometric mean, 2.10, of vacuum and LSGO. High resolution FTIR transmission measurements, corresponding to various laser frequencies[15] were used to confirm the etched thickness.

Another type of broadband AR coatings that may be applied to sample substrates, waveplates, and some detector cold filters is a thin metallic film.[16] The Fresnel reflection coefficient for an interface between vacuum and a thin metallic film on a dielectric of index n is $r = (n-1-Z_0/R_\square)/(n+1+Z_0/R_\square)$ which is zero under the condition that the sheet resistance $R_\square = Z_0/(n-1)$ where $Z_0 = 377\,\Omega$ is the impedance of free space. $R_\square$ is approximately constant provided the scattering rate is substantially greater than the optical frequency, a condition met in the FIR for nichrome (NiCr) films. Such AR coatings on quartz, silicon, gallium arsenide (GaAs), and LSGO were characterized via high resolution FTIR transmission measurements and used successfully in a number of Faraday experiments.

In some very specific circumstances, etalons within the sample can be used to emphasize particular material properties. For example, appropriate engineering of the etalon in TIs allows isolation of the surface state response producing a Faraday signal which exactly equals the fine structure constant.[13] However, in most circumstances, elimination of the etalon is desirable to simplify the optical system and subsequent analysis.

B. Sample design and mounting considerations

Ideally the sample should be made as large as possible and the laser spot as small as possible. However, diffraction limits the minimum spot size at the sample to $1.22\lambda f/D$. For our magnet cryostat, f/D is 3.5 so the spot size for $20\,cm^{-1}$ radiation is 2 mm. Samples much smaller than the spot size can be located within an aperture to reduce the background. However, an aperture introduced at this point in the beam path will cause spurious polarization changes at its edges that can mask the Faraday signals. Constructing the aperture from an absorbing material like graphite reduces such effects.

Many of the samples studied were highly reflective and poorly transmissive. By strategically placing graphite absorbers on the re-entrant copper bore tubes (Fig. 1) and sample stick (Fig. 2), and mounting the sample on an aperture, the effects of beam scatter were measured to be $\sim 5 \times 10^{-5}$ which is negligible in nearly all circumstances. Imaging the sample onto a spatial filter placed at the location of the detector has been used effectively to further attenuate scattering effects. Note that an aperture in this location will not introduce any spurious signal by modifying the polarization since the analyzer polarizer has already decoded the polarization information.

For the simple case of thin film samples, the Faraday angle is related to the Hall angle as shown in Eq. A15 by a factor involving the sheet resistance $1/(\sigma_{xx}d)$ acquired by an independent FTIR spectroscopic measurement. This value may be engineered to be close to 1 by choosing the thickness of the film. However, as shown in Eq. A15, the sheet resistance should be as small as possible while still allowing adequate transmission. As a gauge, samples which attenuated the throughput intensity by four orders of magnitude were successfully measured (like the $Bi_2Sr_2CaCu_2O_{8+x}$ sample deep in the superconducting state as shown in Fig. 5).[9] The signal at this level is detector noise limited.

The sample mounting system must maintain the sample position as well as control the sample temperature. Its central component is a sample stick, which was modified from a design originally made by Oxford Instruments. The cold finger shown in Fig. 2 is cooled by a continuous flow of liquid helium. The sample rests on a 1/16" thick copper plate which has a graphite aperture smaller than the sample. A 100 Ω, 1/4 W metal film resistor epoxied into a slot in the sample plate serves as

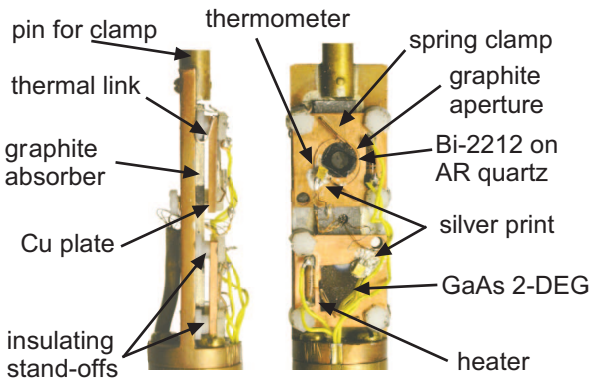

FIG. 2. (Color online) Photographs of the sample stick cold finger depict two views. Total length shown is ∼2.5 inches. The top sample is peeled single crystal $Bi_2Sr_2CaCu_2O_{8+x}$ (Bi-2212) on an AR coated quartz substrate. The bottom sample is a NiCr coated GaAs 2-DEG heterostructure with an AR coating.

a heater. To restrict the motion of the sample during temperature and magnetic field sweeps, a 3" long thin-walled stainless-steel tube is silver soldered to the end of the cold finger. This tube fits into a teflon insert in an aluminum chuck which we added to the cryostat housing. The chuck is actuated from outside the housing. A copper wire serves as a thermal link whose size is adjusted to allow sufficient cooling of the sample while throttling heat flow to the sample stick from the sample heater minimizing thermal expansion effects. The temperature can be continuously varied from 10 to 310 K. Thermal stresses on the sample are minimized while maintaining adequate thermal coupling to the copper plate by mounting the sample with a spring clip on one end and silver epoxy on the other. A Lakeshore 340 temperature controller monitors and regulates the temperature of the sample and simultaneously monitors the temperature of the sample-stick.

C. Magnet

Our magnet is an Oxford Instruments Helmholtz or split coil superconducting magnet that can scan magnetic field between ±8 T in approximately 12 minutes. The magnet is maintained in a liquid helium bath. The vacuum windows are 0.001" thick polyimide which are slightly permeable to helium, allowing a small amount of exchange gas to enter the vacuum chamber. This causes cooling of the polyimide windows resulting in water condensation. This is mitigated by blowing room temperature air constantly across the windows. The entire magnet dewar rests on four 1/4-20 screws to allow height and tilt adjustment for aligning to the optical beam. An Oxford model PS120-10 power supply controls the superconducting magnet current.

D. Laser system

As mentioned earlier, the laser system is a molecular vapor FIR laser pumped by a continuous wave CO_2 laser. The CO_2 laser is a model PL5 from Edinburgh Instruments Ltd. and is tunable from 9 to 11 μm. Its output is a 7.5 mm diameter beam with maximum power of 50 W. The output is focused by an AR-coated ZnSe lens into the cavity of the FIR laser through a small hole in one of the FIR cavity mirrors.

The FIR laser is a home-built dielectric waveguide laser[17,18] with two adjustable flat mirrors on either end. The input coupler is a 2 inch diameter molybdenum flat mirror with a 1.5 mm aperture purchased from SPAWR Industries. The input coupler accommodates a ZnSe Brewster window which minimizes destabilizing back-reflection feedback into the CO_2 laser. The output coupler is a quartz substrate with a silicon dielectric coating grown to a thickness matching a 1/4 wave at 10 μm to provide a high reflectivity for the pump beam. A gold annulus sputtered on the silicon surface defines a 1 cm diameter FIR output aperture. The total area of the output coupler allows the CO_2 beam to be maximally maintained within the FIR laser cavity while concurrently filtering out MIR frequencies from optical elements downstream. The large aperture minimizes diffraction effects. A 1.3 m fused silica tube forms the FIR waveguide and maintains its length. Its low thermal expansion coefficient $7.5 \times 10^{-7}/K$ helps to maintain stability. Diffraction losses strongly attenuate higher order modes[19] while lower order modes are only slightly attenuated due to the grazing incidence with the waveguide.[17,18,20–22] The power output depends strongly on the chosen FIR frequency, but is typically between 1 and 50mW. The axial mode spacing is $\Delta\nu_{ax} = c/(2L) \sim 150$ MHz, the Doppler broadening is ~ 5 MHz for methanol, and pressure broadening is typically $\sim$ 40MHz/torr $\approx$ 4 MHz under the operating pressure of 100 mTorr. Typical gasses used are CD_3OD ($24.6\,cm^{-1}$), CH_3OH ($84.7\,cm^{-1}$), CH_2F_2 ($42.3\,cm^{-1}$), and CH_3OD ($175.4\,cm^{-1}$). A continuous flow at typically ∼100 mTorr pressures is maintained, and a gas handling system with a cold trap is used to recapture the gasses.

The FIR laser lines are scanned for the presence of multiple resonances using a step scan fourier transform polarizing spectrometer. The cyclotron frequency of a calibrated GaAs 2-DEG provides a convenient *in situ* tool to ascertain the FIR laser wavelength (see Sec. IV D).

E. Mechanical Rotator

The high speed mechanical rotator spins an optic of up to 1" diameter at an adjustable speed up to 3000 rpm resulting in a rotator fundamental frequency of 50 Hz. The optic is located within a nominal 1" diameter threaded bore tube. Two threaded rings sandwich the optic between two o-rings that provide cushioning to distribute

stress which would otherwise introduce non-uniformities into the optic. The bore tube is pressed into two ABEC-7 angular contact ball bearings which are themselves pressed into the aluminum rotator housing. An Animatics model SM2315D servomotor with programmable PID feedback drives the bore tube by means of a kevlar reinforced polyurethane timing belt which engages a pulley pressed onto the bore tube end. An intermediate belt tensioner reduces belt slap and jitter. Black paint on a portion of the bore tube pulley provides a target for an optical sensor which supplies the electronic phase reference for the lockin amplifiers. The phase noise as measured on the lockins is within $1:10^4$ (at 50 Hz using a 200 msec time constant).

An array of various thicknesses of x-cut quartz first-order waveplates are chosen to cover the entire spectral region from 3 to 240 cm^{-1}. Whenever the thickness of the waveplate is not optimal resulting in a retardance of $\Delta\beta \neq \pi/2$, signal is sacrificed (see Eq. A2). The limiting upper frequency when using quartz waveplates is $\sim 240\,cm^{-1}$.

F. Detectors, mirrors, polarizers, and beam splitter

The detectors are silicon composite bolometers purchased from Infrared Laboratories. The primary detector is cooled to 2 K and the reference detector to 4 K. The 77K and helium cold stage filters are quartz, the vacuum window is wedged white polyimide, and a Winston cone collects radiation up to an f/# of 3.5. The characteristic frequency response of the primary detector is ≈500 Hz with a noise-equivalent-power of 2×10^{-13} W/Hz$^{1/2}$ at 100 Hz and a responsivity of 2×10^5 V/W.

All 90 degree off-axis parabolic mirrors are 4" aluminum substrates with MgF_2 coatings purchased from Janos technology. Flat mirrors are bare aluminum evaporated on optically flat glass.

Polarizers are evaporated Au on 6 μm thick mylar with 4 μm pitch and 2 μm linewidth purchased from ScienceTech. These are mounted taut between aluminum rings. Their measured extinction coefficient is 10^{-5} at $84.7\,cm^{-1}$.

The reference beam splitter is a 0.00048" thick mylar sheet that is mounted taut between 2 flanges with o-rings. The reflectance is ∼10% at $84.7\,cm^{-1}$ and is slightly frequency dependent.

G. Electronics

The bolometer detectors are equipped with pre-amplifiers that allow a high impedance ($\gg 50\ \Omega$) output at gain settings of 1, 200, or 1000.

The output signal of the transmission bolometer detector is fed into an EG&G 5113 low-noise pre-amplifier which is then fed into a 7280 EG&G lock-in amplifier. A homemade optical encoder reads the frequency of the rotator bore and generates TTL pulses to the lock-in amplifier. The 7280 decomposes the signal into in- and out-of phase components of the second and fourth harmonics. An EG&G 7260 and a EG&G 7265 lock-in amplifier measure the magnitude of the chopped signal from the reference and transmission detectors.

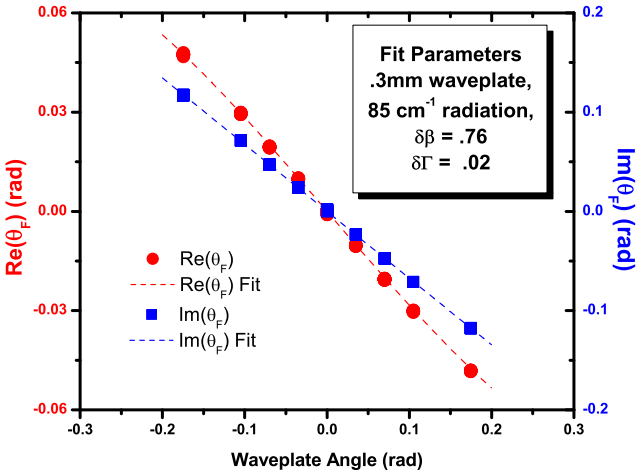

FIG. 3. (Color online) The real and imaginary part of the Faraday angle is measured as a function of angle for a quartz waveplate and fit using the waveplate parameters $\delta\beta$ and $\delta\Gamma$. The imaginary part is calculated using the fit parameters and overlayed on top of the data.

The detectors are nonlinear causing sums and differences of frequencies of various noises and signals to appear in the spectrum. A spectrum analyzer enables choosing ω_{chop} and ω (typically 311 and 49 Hz, respectively) such that the frequencies of interest do not inadvertently overlap with other harmonics or their sums and differences.

An in-house Labview program simultaneously controls and acquires data from the magnet power supply, temperature controller, EG&G 5113 preamplifier, and three lock-in amplifiers.

IV. INSTRUMENT CALIBRATION AND OPERATION

A. Electronics

1. Lock-in amplifiers: harmonic analysis and setting the phase

The complete detector signal is given by Eq. A1 and A2. The EG&G lock-in amplifiers measure the RMS-amplitude of all signals. Optically chopping produces a square wave whose first harmonic amplitude is 0.637 compared to the square wave amplitude. The measured R_{dc} value needs to be multiplied by a factor of 2 since the ac-

tual dc level is the peak-to-peak value of the square waveform. In this case, the magnitude of the chopped signal measured by the lock-in amplifier needs to be multiplied by 2/.637 to be used in Eq. A2 as R_{dc}.

The phase of the 4ω lock-in is set to zero in zero magnetic field. However, inspection of Eq. A2 shows that the 2ω phase can not accurately be set under the same conditions since both the in- and out- of phase signals are close to zero (since $\Delta\Gamma \approx 0$). Conceptually, the 2ω phase can only be set when there exists a substantive $\mathrm{Im}(\theta_F)$ signal such that $A_{o,2\omega} >> A_{i,2\omega}$. Since $\Delta\Gamma$ is small, maximizing $\mathrm{Im}(\theta_F)$ by adjusting the phase of the 2ω signal in magnetic field is, in principle, a good method for setting the phase. In practice, a single lock-in is used to measure both the 2ω and 4ω signals. The phase of the second harmonic is set equal to the phase of the fourth harmonic. In software, the phase of the 2ω channel is then rotated by $\Delta\phi_{2\omega}$ to maximize the $\mathrm{Im}(\theta_F)$ signal. $\Delta\phi_{2\omega}$ is found to be the same for a variety of samples and corresponds to the phase shifts observed when characterizing the frequency dependence (where phase information was acquired) of the detector between the 2ω and 4ω frequencies.

2. Detector frequency roll-off

The relative phase and amplitude response of the detectors and preamplifiers as a function of modulation frequency are experimentally characterized. One method involves double chopping an FIR beam whereby one chopper continuously sweeps frequency while the other remains at fixed frequency. The amplitude response is used to correct the detector signal between the three relevant modulation frequencies: 2ω, 4ω, and ω_{chop}.

B. $\Delta\beta$ and $\Delta\Gamma$ from FTIR spectroscopy

FTIR spectroscopy was performed on waveplates inserted at various angles θ between two parallel polarizers. The transmitted intensity (relative to the input intensity) is given by the following:

$$I(\theta) = e^{-2\gamma_1}\cos^4(\theta) + e^{-2\gamma_2}\sin^4(\theta) + 2e^{-(\gamma_1+\gamma_2)}\cos(\Delta\beta)\sin^2(\theta)\cos^2(\theta)$$

where γ_1 and γ_2 are the absorption along the e- and o-axis of the waveplate, and $\Delta\beta$ is the retardance. Taking ratios of I(θ) for various angles θ, $\Delta\Gamma = \gamma_2 - \gamma_1$ and $\Delta\beta$ as a function of frequency can be derived.

C. $\Delta\beta$ and $\Delta\Gamma$ in situ calibration: polarizer as sample

The preferred method to calibrate waveplates is *in situ* in which the unknown waveplate is inserted into the rotator. Adjusting a polarizer to various angles α inserted immediately downstream from the rotator yields a detector signal given by Eq. A4. After taking ratios of the various amplitudes, there are a total of four equations. If we treat as unknowns the four quantities $\Delta\beta$, $\Delta\Gamma$, and the frequency roll-off of the detector between 2ω and 4ω and between 2ω and ω_{chop}, then simultaneously solving for all four quantities gives an *in situ* calibration of the waveplate parameters and frequency roll-off of the detector. Small polarization errors introduced from imperfections associated with the waveplate (for example, an imperfect AR coating) and/or induced effects from the kapton vacuum windows are corrected with this method by giving an effective $\Delta\beta$ and $\Delta\Gamma$ which is always within $\sim 5\%$ of independent characterizations of the waveplate. The detector frequency roll-off never requires correction of more than small fractions of a percent. An analysis justifying this method of error correcting is detailed in Ref. 23.

The real part of the Faraday angle measured by rotating the polarizer to small angles (± 5 degrees) by Eq. A3 exactly equals α (given by Eq. A4) thus providing a very good absolute calibration of $\mathrm{Re}(\theta_F)$.

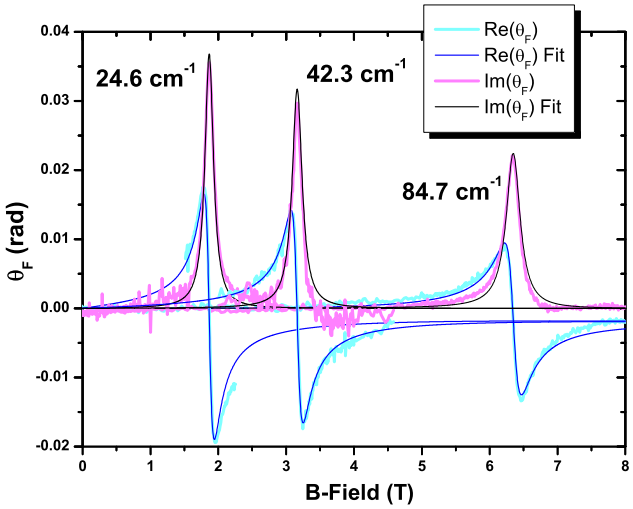

FIG. 4. (Color online) The Faraday angle measured at 3 frequencies as a function of magnetic field for an AR-coated GaAs 2-DEG heterostructure with a 25 $\Omega/\Box$ layer of NiCr at 80 K. The real part of the Faraday angle is fit using the mobility (μ), electron density (n), and NiCr electron scattering rate (γ_{NiCr}) as parameters. For all frequencies, $n = 1.78 \times 10^{15} m^{-2}$ and $\gamma_{NiCr} = 5100\ cm^{-1}$. The mobility was found to be 14, 12, and 8.4 $m^2/Vsec$ for 24.6, 42.6, and 84.7 cm^{-1}, respectively. The GaAs electron mass was taken to be $0.07 \times m_e$.

D. Calibration of Im(θ_F): inserting a waveplate or 2-DEG as a reference sample

By inserting a waveplate immediately downstream from the rotator at various angles α while measuring Re(θ_F) and Im(θ_F) given by Eq. A7, it is possible to calibrate the imaginary part of the Faraday angle with respect to the real part. The inserted waveplate parameters $\Delta\beta'$ and $\Delta\Gamma'$ are obtained by fitting the real part of the Faraday angle. The fit parameters are then used to calculate the imaginary part, and overlayed on the imaginary Faraday angle data. Results for the 84.7 cm^{-1} data using a 0.3 mm thick waveplate is shown in Fig. 3. Waveplates measured at other frequencies were checked in the same manner. The fit parameters of the waveplate agree with other independent waveplate characterizations (Sec. IV B and IV C).

A GaAs 2-DEG sample is used for calibration of the Im(θ_F) as well. Im(θ_F) and Re(θ_F) have a well defined relationship as shown in Eq. A12 allowing calibration of Im(θ_F) with respect to Re(θ_F). A GaAs 2-DEG heterostructure with an AR coating and a 25 $\Omega/\Box$ layer of NiCr on the opposite side of the wafer was deposited in order to attenuate the transmission level to $\sim 1\%$. The transmission level and magnitude of the Faraday signals are similar to many of our experiments. The mobility and the density of electrons are used as fit parameters. The small Faraday response of the NiCr layer is accounted for with a simple Drude model where the electronic scattering rate is a fit parameter.

This sample was used to check the imaginary part of the Faraday angle with respect to the real part at three separate frequencies: 24.6, 42.3, and 84.7 cm^{-1}. The real part was fit, and the imaginary part was then calculated using the fit parameters from the real part. The results are shown in Fig. 4.

The same electron density and NiCr scattering rate were used for all three frequencies, namely $1.78 \times 10^{15}\, m^{-2}$ and $5100\, cm^{-1}$. The mobility is a function of frequency and found to be 14, 12, and 8.4 m^2/ V sec at 24.6, 42.3, and 84.7 cm^{-1}, respectively. The temperature was held at 80 K for all data. Since the mobility is inversely proportional to the effective mass as well as the scattering rate, the data suggest that either the mass or the hall scattering rate is enhanced as the frequency is increased. Since the resonant frequency is not significantly shifted away from the calculated cyclotron frequency ($\propto 1/m$), the frequency dependence is associated with the scattering rate.

All of the data show some small asymmetry about the resonance in the imaginary part of the Faraday angle. This might be a result of some small amount of mixing between the real and imaginary parts of the Faraday angle. Imperfect sample AR coatings will cause etalons leading to some small amount of mixing.

24.6 cm^{-1}		**42.3** cm^{-1}		**84.7** cm^{-1}	
Re(θ_F)	**Im(θ_F)**	**Re(θ_F)**	**Im(θ_F)**	**Re(θ_F)**	**Im(θ_F)**
2.031	0.374	1.992	0.457	1.865	1.081
1.937	0.409	2.074	0.450	1.886	1.105
2.057	0.394	1.992	0.457	1.957	1.067
1.982	0.373	2.035	0.446	1.911	1.097
-.—	-.—	2.051	0.443	-.—	-.—
2.002	0.388	2.029	0.451	1.905	1.088

TABLE I. Slopes of individual magnetic field sweeps in mrad/T performed on Bi-2212 at 100 K like those depicted in Fig. 5(a,b). The last row is the column average.

V. INSTRUMENT PERFORMANCE: MEASUREMENTS ON BI-2212

To illustrate the performance of the instrument, we show reported results[9] on optimally doped single crystal $Bi_2Sr_2CaCu_2O_{8+x}$ (Bi-2212) samples 100 nm thick with an area defined by an aperture 2.5 mm in diameter as shown in Fig. 2. The thin cuprate superconducting crystal was mounted to an AR coated quartz substrate. The longitudinal conductivity σ_{xx} was independently measured via FTIR spectroscopy.

Magnetic field sweeps to ± 8 T were performed at 100 K. Fig. 5(a,b) shows the Faraday angle at 100 K as a function of magnetic field for 10.5 meV (84.7 cm^{-1}) radiation. A compilation of the slopes associated with individual magnetic field scans of both the real and imaginary part of the Faraday angle for all frequencies is presented in Table I.

Temperature sweeps from 100 to 300 K and from 300 to 25 K are shown in Fig. 5(c,d). The transmission changes by two orders of magnitude between high and low temperature since the sample becomes superconducting. Evident in the traces is the growing level of detector noise as temperature is decreased. There exists a temperature dependent background produced by sample movement. Subtracting scans in ± 8 T and dividing by 2 nulls the background signal. The resulting Faraday angle is shown in Fig. 5(e,f) where multiple scans were averaged and then smoothed with a 3 K moving average. Magnetic field sweeps taken at various discrete temperatures give the same value of the Faraday angle as the temperature sweep data.

The current limitation of the signal-to-noise level is imposed by drift produced by sweeping temperature and to a lesser extent from sweeping magnetic field. The current noise from these effects is 0.1 mrad, or 10μrad/T.

Variations of the system are currently underway. dc current measurements which depend upon the chirality of the incident light are planned which utilize the same optical polarization modulation technique.[24] A Kerr geometry is being configured since the technique is sensitive to a single surface, particularly important in measuring

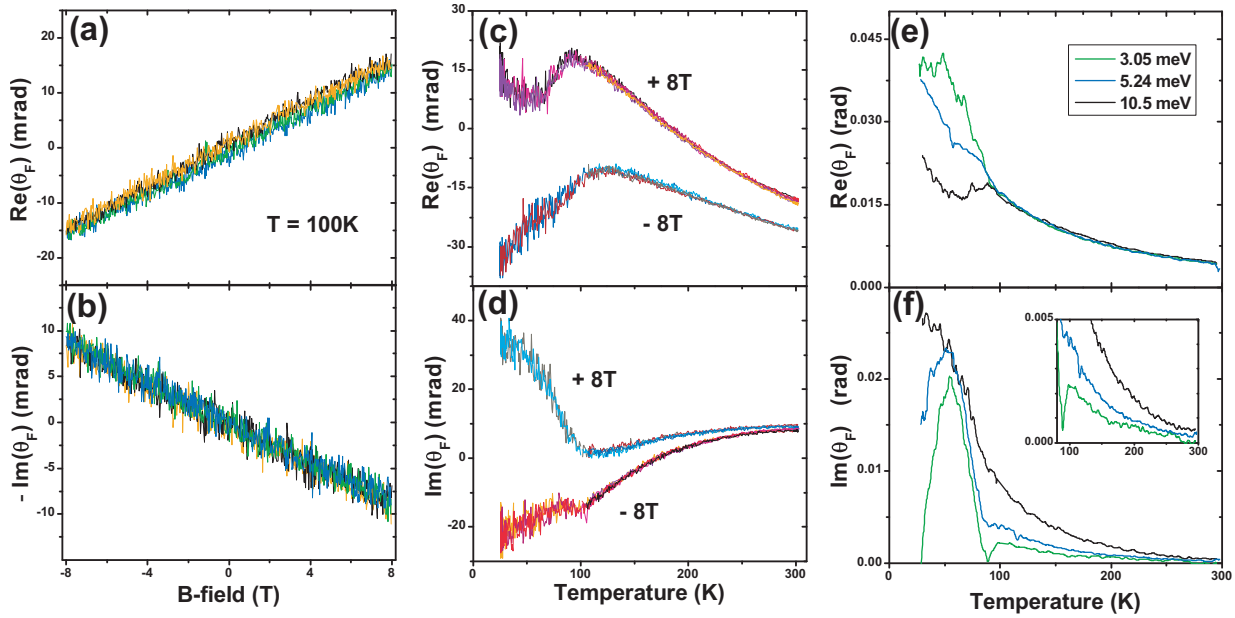

FIG. 5. (Color online) (a,b) Faraday angle measured at 10.5 meV (84.7 cm^{-1}) and 100 K versus B-field. Four scans are depicted. (c,d) Faraday angle measured at ±8 T versus temperature. Ten scans are depicted. (e,f) Faraday angle versus temperature found by subtracting scans in ±8 T, averaging multiple scans together, and performing a 3 K rolling average with temperature.

topological insulators.

ACKNOWLEDGMENTS

The authors extend their thanks to Andrei B. Sushkov, Geoff Evans, and Jeffrey R. Simpson for their assistance in performing the various reported measurements, and Genda Gu and Matthew Grayson for supplying the Bi-2212 and GaAs 2-DEG samples. This work was supported by the CNAM, NSF (DMR-0030112), and DOE (DE-AC02-98CH10886).

Appendix A: Mathematical formalism

1. General Notation

The entire optical system can be described as a series of transfer functions which operate on the initial state of an incident electro-magnetic plane wave.

Dirac notation is used to efficiently keep track of the polarization state as is described in Ref. 25 and Ref. 11. Under our convention whereby the radiation propagation is in the positive z direction, the electric polarization vector $|E\rangle$ can be represented in either a linear (L) or circular (C) polarization basis as:

$$\langle L|E\rangle = \begin{pmatrix} E_x \\ E_y \end{pmatrix} \text{ and } \langle C|E\rangle = \begin{pmatrix} E_+ \\ E_- \end{pmatrix}$$

where $E_\pm = E_x\hat{x} \pm iE_y\hat{y}$. E_+ then represents the circular polarization with the electric field rotating in a positive direction about the z axis in the lab frame. The main types of optical components of our system are: polarizer (P), waveplate (WP), and sample (S), which may be represented as follows:

$$\begin{aligned} \langle L|P|L\rangle &= \begin{pmatrix} 1 & 0 \\ 0 & 0 \end{pmatrix} \\ \langle L|WP|L\rangle &= \begin{pmatrix} e^{i\beta_1-\Gamma_1} & 0 \\ 0 & e^{i\beta_2-\Gamma_2} \end{pmatrix} \\ \langle L|S|L\rangle &= \begin{pmatrix} t_{xx} & t_{xy} \\ t_{yx} & t_{yy} \end{pmatrix} \end{aligned}$$

$\Delta\beta = \beta_1 - \beta_2$ and $\Delta\Gamma = \Gamma_1 - \Gamma_2$ are the differential phase shift and absorption between linearly polarized light along the ordinary and extra-ordinary optical axis of the waveplate. For an ideal quarter waveplate $\Delta\beta = \frac{\pi}{2}$ and $\Delta\Gamma = 0$. Actual values are experimentally determined by an *in situ* calibration technique (Sec. IV C) and verified by FTIR measurements (Sec. IV B). t_{xx}, t_{xy}, t_{yx}, and t_{yy} are the transmission amplitudes for an arbitrary sample. Most of the measured samples are rotationally invariant meaning that $t_{xx} = t_{yy}$ and $t_{xy} = -t_{yx}$. In this case:

$$\langle L|S_0|L\rangle = \begin{pmatrix} t_{xx} & t_{xy} \\ -t_{xy} & t_{xx} \end{pmatrix}$$

The rotation of a component by an angle ϕ may be represented by an arbitrary angle ϕ clockwise by the following operator:

$$\langle L|R(\phi)|L\rangle = \begin{pmatrix} \cos\phi & -\sin\phi \\ \sin\phi & \cos\phi \end{pmatrix}$$

A rotating quarter-waveplate spinning at an angular frequency ω about the positive z axis is represented by:

$$\langle L|RWP(\omega)|L\rangle = \langle L|R(\omega t)|L\rangle\langle L|WP|L\rangle\langle L|R(-\omega t)|L\rangle$$

2. Detector Signal Analysis

a. Rotationally invariant Sample

Using the above notation, the intensity at the output detector of the system shown in Fig. 1, for a rotationally invariant sample is:

$$\begin{aligned} I_D &= |\langle L|P|L\rangle\langle L|S_0|L\rangle\langle L|RWP(\omega)|L\rangle\langle L|P|L\rangle\langle L|E_0\rangle|^2 \\ &= R_{dc} + A_{o,2\omega}\sin 2\omega t + A_{i,2\omega}\cos 2\omega t \\ &\quad + A_{o,4\omega}\sin 4\omega t + A_{i,4\omega}\cos 4\omega t \end{aligned} \tag{A1}$$

where,

$$\begin{aligned} R_{dc} &= e^{-\Gamma}|t_{xx}|^2\frac{1}{4}((1-|\tan\theta_F|^2)\cos\Delta\beta + \\ &\qquad (3+|\tan\theta_F|^2)\cosh\Delta\Gamma) \\ A_{o,2\omega} &= e^{-\Gamma}|t_{xx}|^2(Im(\tan\theta_F)\sin\Delta\beta + \\ &\qquad Re(\tan\theta_F)\sinh\Delta\Gamma) \\ A_{i,2\omega} &= -e^{-\Gamma}|t_{xx}|^2\sinh\Delta\Gamma \\ A_{o,4\omega} &= e^{-\Gamma}|t_{xx}|^2\frac{1}{2}Re(\tan\theta_F)(\cos\Delta\beta-\cosh\Delta\Gamma) \\ A_{i,4\omega} &= e^{-\Gamma}|t_{xx}|^2\frac{1}{4}(|\tan\theta_F|^2-1)(\cos\Delta\beta-\cosh\Delta\Gamma) \end{aligned} \tag{A2}$$

.

$A_{i,2\omega}$, $A_{o,2\omega}$, $A_{i,4\omega}$, $A_{o,4\omega}$ are the second and fourth harmonic signals on the output detector that are in-phase (i) and out-of-phase (o) with the original harmonic signal that results when no sample is present or when the magnetic field is zero. By taking various ratios of the measured quantities in Eq. A2, one may extract the quantities $\mathrm{Re}(\tan\theta_F)$ and $\mathrm{Im}(\tan\theta_F)$.

In many circumstances, t_{xy} is zero in zero magnetic field and remains small even up to the maximum magnetic field such that $|t_{xy}|^2 \ll |t_{xx}|^2$. In this small angle limit, the Faraday angle may be obtained from Eq. A2:

$$\begin{aligned} Re(\theta_F)_1 &= -\frac{1}{2}\frac{A_{o,4\omega}}{A_{i,4\omega}} \\ Re(\theta_F)_2 &= \frac{1}{2}\frac{\cos\Delta\beta+3\cosh\Delta\Gamma}{\cos\Delta\beta-\cosh\Delta\Gamma}\frac{A_{o,4\omega}}{R_{dc}} \\ Im(\theta_F)_1 &= \frac{-Re(\theta_F)\sinh\Delta\Gamma}{\sin\Delta\beta} + \\ &\qquad \frac{1}{4}\frac{\cos\Delta\beta+3\cosh\Delta\Gamma}{\sin\Delta\beta}\frac{A_{o,2\omega}}{R_{dc}} \\ Im(\theta_F)_2 &= \frac{-Re(\theta_F)\sinh\Delta\Gamma}{\sin\Delta\beta} + \\ &\qquad \frac{1}{4}\frac{\cosh\Delta\Gamma-\cos\Delta\beta}{\sin\Delta\beta}\frac{A_{o,2\omega}}{A_{i,4\omega}} \end{aligned} \tag{A3}$$

The preferred ratios for evaluating the Faraday angle involve the second and fourth harmonic amplitudes. The corrections involving the detector frequency dependence become more sever for the case of R_{dc} due to the comparatively high chopping frequency.

b. Polarizer or waveplate as a sample

Inserting a polarizer at an angle α with respect to the analyzer in place of the sample, and replacing the rotationally invariant sample in Eq. A1 with $\langle L|SP(\alpha)|L\rangle = \langle L|R(\alpha)|L\rangle\langle L|P|L\rangle\langle L|R(-\alpha)|L\rangle$ yields the following detector signal:

$$\begin{aligned} R_{dc} &= \frac{e^{-\Gamma}}{4}\cos^2\alpha\ (\cos 2\alpha\cos\Delta\beta + (2+\cos 2\alpha)\cosh\Delta\Gamma) \\ A_{o,2\omega} &= -\frac{e^{-\Gamma}}{2}\cos^2\alpha\ \sin 2\alpha\sinh\Delta\Gamma \\ A_{i,2\omega} &= -\frac{e^{-\Gamma}}{2}\cos^2\alpha\ (1+\cos 2\alpha)\sinh\Delta\Gamma \\ A_{o,4\omega} &= -\frac{e^{-\Gamma}}{4}\cos^2\alpha\ (\cos\Delta\beta-\cosh\Delta\Gamma)\sin 2\alpha \\ A_{i,4\omega} &= -\frac{e^{-\Gamma}}{4}\cos^2\alpha\ (\cos\Delta\beta-\cosh\Delta\Gamma)\cos 2\alpha \end{aligned} \tag{A4}$$

Notice that $A_{o,4\omega}/A_{i,4\omega} = \tan 2\alpha$.

Inserting a waveplate in place of the sample defined by a retardance and differential absorption given by $\Delta\beta'$ and $\Delta\Gamma'$, respectively, whose ordinary axis is at an angle α with respect to the analyzer yields the following transfer function

$$\langle L|SWP(\alpha)|L\rangle = \langle L|R(\alpha)|L\rangle\langle L|WP|L\rangle\langle L|R(-\alpha)|L\rangle \tag{A5}$$

Replacing $\langle L|S_0|L\rangle$ with $\langle L|SWP(\alpha)|L\rangle$ in Eq. A1 yields detector amplitudes in terms of $\Delta\beta'$, $\Delta\Gamma'$, α, $\Delta\beta$, and $\Delta\Gamma$.

We make the following definition:

$$\langle L|SWP(\alpha)|L\rangle \equiv \begin{pmatrix} t'_{xx} & t'_{xy} \\ t'_{yx} & t'_{yy} \end{pmatrix} \tag{A6}$$

With this definition, $t'_{xy} = t'_{yx}$, and if $\Delta\Gamma'$ is sufficiently small, then $t'_{yy} \approx t'_{xx}$. Under these circumstances, the Faraday angle may be derived from the sample waveplate parameters:

$$\begin{aligned} Re(\theta_F) &= \frac{1}{2}(1-\frac{|t'_{xy}|^2}{|t'_{xx}|^2})\frac{A_{o,4\omega}}{A_{i,4\omega t}} \\ Im(\theta_F) &= -\frac{Re(\theta_F)\sinh\Delta\Gamma}{\sin\Delta\beta} + \\ &\qquad \frac{1}{4}(1-\frac{|t_{xy'}|^2}{|t'_{xx}|^2})\frac{\cos\Delta\beta-\cosh\Delta\Gamma}{\sin\Delta\beta}\frac{A_{o,2\omega}}{A_{i,4\omega}} \end{aligned} \tag{A7}$$

where $|t'_{xy}|^2/|t'_{xx}|^2$ is given by

$$\frac{\frac{1}{2}(\cosh\Delta\Gamma'-\cos\Delta\beta')\sin^2 2\alpha}{e^{-\Delta\Gamma'}\cos^4\alpha + e^{\Delta\Gamma'}\sin^4\alpha + \frac{1}{2}\cos\Delta\beta'\sin^2 2\alpha} \tag{A8}$$

3. Faraday angle from a Drude thin film sample

A Drude response in magnetic field is derived by using the classical force equation $q\vec{E} + \frac{q}{c}\vec{v}\times\vec{B} - \frac{m}{\tau}\vec{v} = m\frac{d\vec{v}}{dt}$

together with the definition of current $\vec{J} = nq\vec{v} = \tilde{\sigma}\vec{E}$. The conductivity tensor is diagonal when represented in the circular polarization basis:

$$\langle C|\sigma|C\rangle = \begin{pmatrix} \frac{nq^2}{m}\frac{1}{\gamma - i(\omega-\omega_c)} & 0 \\ 0 & \frac{nq^2}{m}\frac{1}{\gamma - i(\omega+\omega_c)} \end{pmatrix} \equiv \begin{pmatrix} \sigma_+ & 0 \\ 0 & \sigma_- \end{pmatrix} \tag{A9}$$

Since the matrix relating $\vec{J}$ and $\vec{E}$ is diagonal, the complex Fresnel transmission coefficient for a plane wave at normal incidence from vacuum through a thin conducting film ($\lambda \gg$ film thickness) on a semi-infinite substrate of index n can be written as:

$$t_\pm = \frac{2}{1 + n + Z_0\sigma_\pm d} \tag{A10}$$

where $Z_0 = 377\ \Omega/\square$ is the impedance of free space, and d is the thickness of the film.

Utilizing the following conversions,

$$\begin{aligned} \sigma_\pm &= \sigma_{xx} \pm i\ \sigma_{xy} \\ t_\pm &= t_{xx} \pm i\ t_{xy} \end{aligned} \tag{A11}$$

and combining Eq. A9 and A10 gives:

$$\tan\theta_F = -\frac{t_{xy}}{t_{xx}} = -\frac{\kappa\omega_c}{(\gamma - i\omega)(\gamma + \kappa - i\omega) + \omega_c^2} \tag{A12}$$

where $\kappa = \frac{nq^2}{m}Z'$, $\omega_c = \frac{q\,B}{m\,c}$, $Z' = d\ Z_0/(n+1)$, $Z_0 = 377\ \Omega/\square$, n is the index of the substrate, and d is the film thickness. κ is a frequency which characterizes the radiation damping of the 2-DEG, a plasma mode which takes into account the reduction of the electric field inside the medium.

Two-dimensional electron gas heterostructures are usually characterized in terms of the electron mobility and electron density. The mobility can be defined as:

$$\mu \equiv \frac{q}{m}\frac{1}{\gamma} \tag{A13}$$

Inverting Eq. A13 and substituting γ into Eq. A12 gives the Faraday angle in terms of mobility.

4. Converting from Faraday angle to Hall angle in the thin film limit

The Hall angle is defined as:

$$\tan\theta_H \equiv \frac{\sigma_{xy}}{\sigma_{xx}} \tag{A14}$$

Assuming a rotationally invariant sample in the thin-film limit, and converting Eq. 1 to the circular basis via Eq. A11 and using Eq. A10 gives:

$$\tan\theta_F = i\ \frac{t_+ - t_-}{t_+ + t_-} = i\ Z'\ \frac{\sigma_- - \sigma_+}{2 + Z'(\sigma_+ + \sigma_-)}$$

Converting the conductivity back into the linear polarization basis (Eq. A11) and simplifying gives:

$$\tan\theta_F = Z'\ \frac{\sigma_{xy}}{1 + Z'\sigma_{xx}} = \frac{1}{(Z'\sigma_{xx}d)^{-1} + 1}\ \frac{\sigma_{xy}}{\sigma_{xx}}$$

Substituting the definition of the Hall angle (Eq. A14) and rearranging yields the desired result:

$$\tan\theta_H = \left(1 + \frac{n+1}{Z_0\ \sigma_{xx}\ d}\right)\tan\theta_F \tag{A15}$$

[1] D. C. Schmadel, G. S. Jenkins, J. J. Tu, G. D. Gu, H. Kontani, and H. D. Drew, Phys. Rev. B, **75**, 140506 (2007).
[2] H. Kontani, Rep. Prog. Phys., **71**, 026501 (2008).
[3] H. D. Drew and P. Coleman, Phys. Rev. Lett., **78**, 1572 (1997).
[4] A. Zimmers, L. Shi, D. C. Schmadel, W. M. Fisher, R. L. Greene, H. D. Drew, M. Houseknecht, G. Acbas, M.-H. Kim, M.-H. Yang, J. Cerne, J. Lin, and A. Millis, Phys. Rev. B, **76**, 064515 (2007).
[5] J. Cerne, M. Grayson, D. C. Schmadel, G. S. Jenkins, H. D. Drew, R. Hughes, J. S. Preston, and P. Kung, Phys. Rev. Lett., **84**, 3418 (2000).
[6] M. Grayson, J. Cerne, D. C. Schmadel, G. S. Jenkins, H. D. Drew, R. Hughes, J. S. Preston, and P. Kung, J. of Low Temp. Phys., **117**, 1055 (1999).
[7] G. S. Jenkins, D. C. Schmadel, P. L. Bach, R. L. Greene, X. Béchamp-Laganière, G. Roberge, P. Fournier, and H. D. Drew, Phys. Rev. B, **79**, 224525 (2009).
[8] G. S. Jenkins, D. C. Schmadel, P. L. Bach, R. L. Greene, X. Béchamp-Laganière, G. Roberge, P. Fournier, H. Kontani, and H. D. Drew, Phys. Rev. B, **81**, 024508 (2010).
[9] G. S. Jenkins, D. C. Schmadel, A. B. Sushkov, G. D. Gu, H. Kontani, and H. D. Drew, "Terahertz hall measurements on optimally doped single crystal bi-2212," (2010), (in preparation).
[10] L. B. Rigal, D. C. Schmadel, H. D. Drew, B. Maiorov, E. Osquiguil, J. S. Preston, R. Hughes, and G. D. Gu, Phys. Rev. Lett., **93**, 137002 (2004).
[11] J. Cerne, D. C. Schmadel, L. B. Rigal, and H. D. Drew, Rev. Sci. Instrum., **74** (2003).
[12] X. Qi, T. L. Hughes, and S. Zhang, Phys. Rev. B, **78**, 195424 (2008).
[13] J. Maciejko, X. Qi, H. D. Drew, and S. Zhang, (2010), cond-mat/1004.2514.
[14] T. Morimoto, Y. Hatsugai, and H. Aoki, Physica E, **42**, 751 (2010).
[15] A. Spizler, G. S. Jenkins, D. C. Schmadel, and H. D. Drew, "Preparation of removable dielectric ar coatings," (unpublished).
[16] S. W. McKnight, K. P. Stewart, H. D. Drew, and K. Moorjani, Infrared Physics, **27**, 327 (1987).
[17] D. T. Hodges, Infrared Physics, **18**, 375 (1978).
[18] J. J. Dugnan, Appl. Phys., **33**, 1 (1976).
[19] T. Sawatari and N. S. Kapany, J. Opt. Soc. Am., **66**, 362 (1976).
[20] P. Schwaller, H. Steffen, J. F. Moser, and F. K. Kneubuhl, Appl. Opt., **6**, 827 (1967).
[21] S. Jacobsson, Infrared Physics, **29**, 853 (1989).
[22] M. Rosenbluh, R. J. Temkin, and K. J. Button, Appl. Opt., **15**, 2635 (1976).
[23] G. S. Jenkins, *IR Hall angle measurements on Single Crystal $Bi_2Sr_2CaCu_2O_{8+\delta}$*, Ph.D. thesis, University of Maryland, College Park (2003).
[24] J. E. Moore and J. Orenstein, (2009), cond-mat/0911.3630.
[25] D. Schmadel, *The ac- Hall Effect in Single Crystal $Bi_2Sr_2CaCu_2O_{8+\delta}$*, Ph.D. thesis, University of Maryland, College Park (2002).